Effect of Engineered Cracks in Catalyst Layers on PEMFC Catalyst Layer Durability

*ChungHyuk Lee[1,2], Siddharth Komini Babu[1], Brian M. Patterson[3], Kimberly S. Reeves[4], Haoran Yu[4], David A. Cullen[4], Rangachary Mukundan[1,5], Rod L. Borup[1], and Jacob S. Spendelow[1]***

[1] Materials Physics and Applications Division, Los Alamos National Laboratory, Los Alamos, NM, USA

[2] Department of Chemical Engineering, Toronto Metropolitan University, Toronto, ON, Canada

[3] Materials Science and Technology Division, Los Alamos National Laboratory, Los Alamos, NM, USA

[4] Center for Nanophase Materials Sciences, Oak Ridge National Laboratory, Oak Ridge, TN, USA

[5] Present address: Energy Technologies Area, Lawrence Berkeley National Laboratory, Berkeley, CA, USA

Keywords: hydrogen fuel cell; electrode; catalyst layer; cracks; durability; carbon corrosion

*email: spendelow@lanl.gov

Abstract

Proton exchange membrane fuel cells (PEMFCs) are expected to play a pivotal role in decarbonizing the transportation sector, and particularly heavy-duty vehicles (HDVs). However, improvements in durability are needed for PEMFCs to compete with state-of-the-art power sources for HDVs. Here, we examine how catalyst layer (CL) cracks that are engineered affect the CL durability by using patterned silicon templates to control the CL crack density at the micrometer scale. Electrochemical analyses show that the initial PEMFC performance is relatively unaffected by crack density, but the performance after durability testing was strongly affected. Specifically, CLs with high crack density showed higher performance relative to CLs without cracks after application of a carbon corrosion accelerated stress test. Electrochemical analyses coupled with X-ray computed tomography and scanning transmission electron microscopy with energy dispersive X-ray spectroscopy showed that the cracks provide shorter oxygen diffusion pathways to reaction sites, leading to decreased oxygen transport resistance.

Additionally, we observed that the catalyst durability is unaffected by cracks. Our results provide a mechanistic explanation of the role of cracks in CL durability.

Introduction

Interest in proton exchange membrane fuel cells (PEMFCs) is rapidly growing[1] due to their potential to decarbonize heavy duty vehicles (HDVs). PEMFC-powered HDVs have relatively short refueling time and provide driving range similar to that of conventional combustion-powered HDVs, while also providing high efficiency (greater than 60%) and emissions-free operation.[2] Research efforts in PEMFCs are increasingly focusing on HDV applications, with particular emphasis on durability, since HDV applications demand ~7.5 times higher lifetime driving range compared to light duty vehicles.[2] This enhanced durability requirement affects catalyst layers (CLs) (catalysts,[3–6] supports,[7,8] and ionomers[9–11]), membranes,[12–14] gas diffusion layers,[15,16] and flow fields.[17] While many of the degradation mechanisms can be suppressed using system operation strategies, operating conditions are also directly correlated to PEMFC performance[18] and hence limits the practical applicability of such strategies. Thus, materials development (particularly in CL structure) remains critical for reducing system cost, providing fault tolerance, and improving lifetime.[19]

One of the main challenges in PEMFC durability is the formation and growth of cracks in CLs. Cracks can develop from many sources including catalyst ink ageing,[20] ink coating and drying processes,[21] poor handling,[22] start-up/shutdown cycles,[23,24] freeze-thaw cycles,[25] carbon corrosion,[26] and mechanical strain or defects in the microporous layer and membrane.[27,28] Crack networks in catalyst layers are inherently random in structural properties (such as shapes,[21] density,[29] and width[30]) due to the fabrication process, and previous works have identified ways to mitigate cracks including mechanical reinforcements,[31] thicker catalyst layers,[32] gas diffusion layers (GDLs) with low surface roughness,[33] and bonding of catalyst layer with the GDL.[34] Cracks in CLs have been reported to cause negative repercussions such as membrane crack development (although membrane cracks don't exclusively grow due to CL cracks[35]) and reduced in-plane electrical conductivity,[36] but also positive effects such as enhanced liquid water and oxygen transport.[37] While it is clear that the presence of cracks has a significant effect on fuel cell performance and durability, the role of crack morphology and density is relatively unknown, owing to the difficulty of controlling the inherently random nature of crack formation processes. Specifically, previous crack control methods rely on changing the water/alcohol ratio in catalyst inks[21] or adding small amounts of polymer additives to the catalyst ink,[38] but these methods did not demonstrate full and independent control of crack width, shape, and density. Independent control of crack features is an important first step in understanding crack effects on PEMFC durability.

Here, we developed an experimental platform for precise creation and control of CL cracks using microfabricated templates,[39] enabling detailed investigation of the effects of cracks on PEMFC performance and durability. Specifically, rather than studying real cracks with a random crack network, we use *engineered cracks* with controlled morphological properties to model real cracks. These engineered cracks are useful since real cracks inherently feature non-uniform width, orientation, depth, connectivity, and density, and convolutes our fundamental understanding of crack effects. We selectively controlled the crack density by transferring a CL from a micropatterned decal substrate to a membrane, and subsequently subjected the resulting MEA to extensive testing steps, including a carbon corrosion AST. We observed that crack density had negligible effect on the cell performance at the beginning of test (BOT), but CLs with higher crack density exhibited relatively higher performance at the end of test (EOT). We established that the electrochemical surface area, high frequency resistance, mass activity, and carbon corrosion rate were relatively unaffected by crack density, but the oxygen transport resistance at EOT was significantly lower for the CLs with cracks. X-ray computed tomography (CT) and scanning transmission electron microscopy (STEM) with energy dispersive spectroscopy (EDS) analysis showed that, despite CL thinning and compaction during the carbon corrosion AST, CL cracks persisted at EOT. These cracks shorten the overall oxygen diffusion length to the reaction sites relative to crack-free CLs, and thereby provide higher EOT performance in degraded and compacted CLs. Our findings provide a mechanistic explanation of the role of crack density in controlling performance degradation and inform CL design strategies to enhance performance and durability of PEMFCs.

Experimental

Template and Catalyst Layer Fabrication

We used a template-based approach to control cracks in CLs, as reported in our previous work.[39] In brief, we used photolithography and deep reactive ion etching to fabricate silicon templates with controlled ridge height, width, and spacing. These silicon templates were then coated with a catalyst ink using a Mayer rod-based coating method. The catalyst ink was composed of 34 wt.% Pt on high surface area carbon (TEC10E40E, Tanaka Precious Metals), Nafion ionomer (D2020, Chemours), and isopropanol:water mixture (12:1 volume ratio). The ionomer-to-carbon ratio (I/C) for the cathode CL was 0.9. Each template was coated with the catalyst ink until a Pt loading of 0.3 mg Pt cm^{-2} was achieved. The measured loadings were within ±5% of the target loading for all CLs, as determined by X-ray fluorescence measurements (Quant'X EDXRF, Thermo Fisher Scientific). For the anode CL, we directly coated the anode catalyst ink (10 wt.% Pt (TEC10V20E), I/C 0.5, n-propanol–water (4:3, v/v)) onto a membrane (NR-

211, Chemours) using an ultrasonic spray coater (ExactaCoat, Sono-Tek), with a Pt loading of 0.1 mg Pt cm^{-2}. The active area was 5 cm^2.

After completing the catalyst coating, each cathode CL-coated template was hot-pressed to the anode CL-coated membrane at 1.3×10^3 Pa and 130 °C for 5 minutes for the cathode CL transfer to the membrane. Each membrane with hot-pressed CL and template was then immersed in 1 M NaOH until the silicon template detached from the membrane and CL. After detachment, the resulting membrane electrode assemblies (MEAs) were re-protonated in 0.5 M H_2SO_4 at 70 °C for 2 hours. The baseline CLs were made using the same process, but a flat silicon template was used, yielding a CL with minimal cracking. Readers are referred to our previous work[39] for further details on the CL fabrication procedure.

Catalyst Layer Characterization

Micro CT imaging was completed on the two membranes using a Carl Zeiss X-ray Microscopy Inc. (Pleasanton, CA) Xradia 520 Versa. Samples were extracted from the film with a fresh blade and attached to the head of a nail using cyanoacrylate glue. The micro CT instrument was operated at 50 kVp, 4W, 2401 radiographs, 35 s exposure each, and a 0.45 micrometer voxel size using the 20X objective. The radiographs were collected as the sample was rotated 360°. The tomographic data sets were reconstructed in TXM Reconstructor (Zeiss). The slices were rendered and analyzed in Avizo for Industrial Inspection (Thermo Scientific). The membrane was segmented and converted to a surface. The surface thickness was measured by growing a sphere from the center of every tetrahedron of the surface until it touched another tetrahedron. The CL morphological properties (i.e., crack width, CL thickness) was measured via ImageJ.[40]

To perform scanning transmission electron microscopy (STEM) analysis of the catalyst layer cross section, a portion of each MEA was embedded in epoxy resin and cut by diamond-knife ultramicrotomy, targeting a thickness of 75 nm for each slice. High-angle annular dark-field (HAADF) and EDS images were recorded using a Talos F200X transmission electron microscope (TEM) (Thermo Fisher Scientific) operated at 200 kV and equipped with Super-X EDS system. The EDS data was processed by Esprit software (Bruker). We also performed imaging of the MEAs without embedding in epoxy resin using an SEM system (Thermo Scientific Quattro SEM).

PEMFC Assembly and Testing

The MEAs were assembled in a differential cell (design reported by Baker et al.[41]) and tested using a commercial fuel cell test station (850 Fuel Cell Test Station, Scribner Associates Inc.). We used a microporous layer-coated gas diffusion layer (SGL 22BB, SGL Carbon) on both anode and cathode, and polyurethane gaskets to seal both sides. The MEAs were conditioned using a break-in protocol based on the procedure developed by General Motors.[42]

After break-in, we performed a series of electrochemical tests to characterize the performance of the fuel cell. Polarization curves were performed under H_2/Air (1000/3000 sccm) at 100% RH, 150 kPa_{abs}, and 80°C. We held constant voltages from 0.4 V to open circuit voltage for four minutes at each step and reported the average current during the last minute of each step. We simultaneously measured the high frequency resistance (HFR) at 5 kHz (also reported based on an average over the last minute of each step). Mass activity (MA) was measured under H_2/O_2 (1000/3000 sccm) at 100% RH, 150 kPa_{abs}, and 80°C. We held a constant HFR-corrected voltage of 0.9 V for 15 minutes and determined the MA based on the average current density during the last minute. Electrochemical surface area (ECSA) was determined via cyclic voltammetry from 0.08 to 0.98 V at a sweep rate of 50 mV/s. Cyclic voltammetry was performed with flowing H_2 on the anode (1000 sccm) and stagnant N_2 on the cathode at 150 kPa_{abs} and 35°C cell temperature, with anode and cathode humidifiers at 80°C. Limiting current measurements were performed at 60% RH and 80°C by varying the cell voltage from 0.4 to 0.1 V under H_2/0.5% O_2 in N_2 (500/5000 sccm) at 8 pressure steps ranging from 100 to 275 kPa_{abs}.

The carbon corrosion AST was performed following the USDRIVE Fuel Cell Technical Team Roadmap protocol,[43] which consists of triangle wave voltage cycling between 1.0 and 1.5 V at 500 mV/s. The AST was performed for up to 1000 cycles under H_2/N_2 (200/200 sccm) at 100% RH, atmospheric pressure, and 80°C. The carbon dioxide concentration in the cathode effluent during the AST was measured using a non-dispersive infrared detector (Model 600-NDIR, California Analytical Instruments). Polarization curves, MA, and ECSA were measured after 500 and 1000 AST cycles, with 1000 cycles defined as EOT. The break-in procedure was repeated before performance characterization to recoup recoverable losses. We also performed a catalyst AST, in which the potential was cycled 60,000 times from 0.6 to 0.95 V in a trapezoidal wave with 0.5 s ramp and 2.5 s hold for each potential step, under H_2/N_2 (200/200 sccm) at 100% RH, 150 kPa_{abs}, and 80°C (also based on the USDRIVE Fuel Cell Technical Team Roadmap protocol[43]).

Results and Discussion

Crack effects on catalyst layer carbon corrosion

The morphology of the as-prepared CLs with induced cracks was evaluated via SEM, as shown in **Figure 1**. The top view shows that our method yields precise control of crack formation. Although cracks that naturally form during an ink drying process or a degradation process have a range of shapes including I, V, T, and Y shapes,[21] the cracks reported here are straight, ordered, and controlled in width and spacing, providing a platform for precise understanding of crack morphology effects on fuel cell performance and durability. However, we note that the templating method used here can also be used for creating a realistic crack network by creating a silicon template based on an image of a catalyst layer with real cracks. We denote the CLs as A µm/B µm, where A and B refer to the top width of the cracks and the distance between cracks (measured via SEM), respectively. Crack top width was reduced for the 2 µm/6 µm CL to keep the CL thickness relatively similar across all CLs.

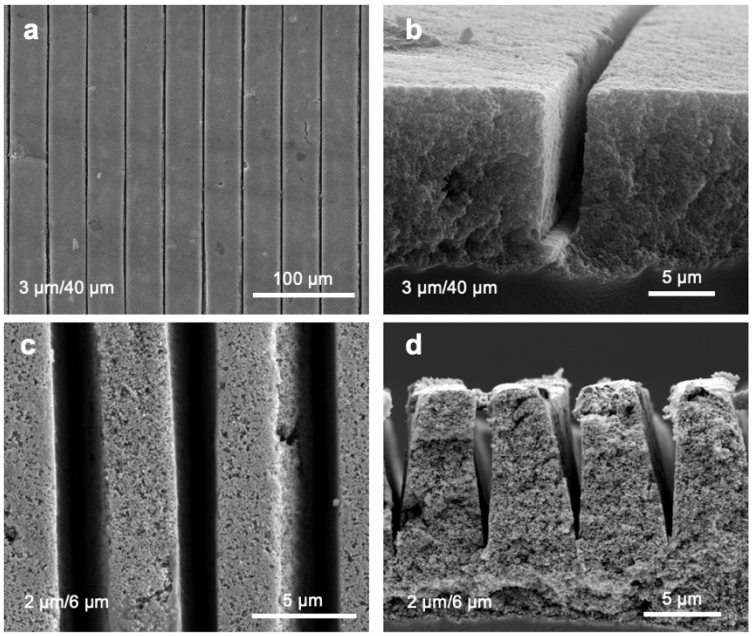

Figure 1. SEM images of catalyst layers with engineered cracks. (a) top and (b) cross-sectional view of 3 µm/40 µm and (c) top and (d) cross-sectional view of 2 µm/6 µm.

The baseline catalyst layer did not feature any noticeable cracks, as it can be seen on the cross-section images in **Figure S1a**. The baseline catalyst layer was relatively free of cracks, which can be attributed to (1) alcohol-rich catalyst ink (92% by volume) allowing the catalyst particles to be relatively well dispersed during the drying process (retention of dispersant during the drying process has been shown to govern crack formation during catalyst manufacturing[44]), and (2) the hot-pressing procedure during the catalyst layer decal transfer process can promote closing of cracks (observed for microporous layer cracks[45]).

Polarization analyses showed that the cracks had a negligible effect on the BOT performance (**Figure 2**). Previous studies reported positive effects of cracks on oxygen and liquid water transport,[37,46] since cracks were hypothesized to act as preferential liquid water transport pathways and suppress liquid water flooding within smaller pores of the CL (similar to the role of cracks in microporous layers[47]). In the present study, we observed the benefits of cracks on the BOT performance only when the CL was deliberately designed to have poor mass transport properties, such as ~3 times thicker CLs with low Pt weight ratio (**Figure S2**) or high ionomer content CLs.[39] Our results demonstrate that bulk O_2 transport resistance through the CL structure has an insignificant contribution to the BOT cell performance under the range of conditions studied, and thus the effect of cracks on BOT performance is also insignificant.

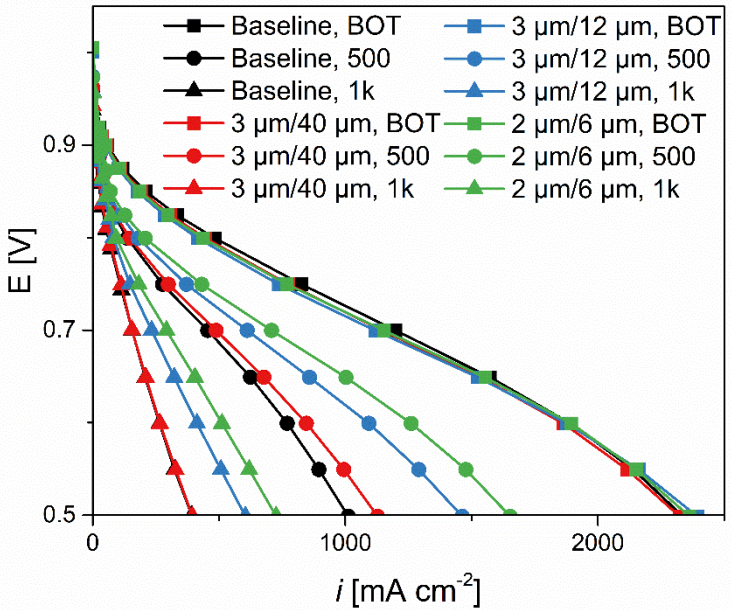

Figure 2. Polarization curves of catalyst layers with and without engineered cracks during carbon corrosion AST. Polarization curves were collected under H_2/Air, 1000/3000 sccm, 100% RH, 150 kPa_{abs}, and 80°C.

On the contrary, we observed a different effect of cracks on performance after application of carbon corrosion ASTs (**Figure 2**). Specifically, after the CLs underwent carbon corrosion, CLs with higher crack density exhibited relatively less loss in performance compared to CLs with low crack density. Comparing 2 μm/6 μm and the baseline CL, the current density at 0.7 V was 55% higher after 500 cycles and 87% higher after 1000 cycles for the 2 μm/6 μm CL (See **Figure S2** for repeated data). To elucidate the cause of the higher EOT performance in cracked electrodes, we examined the HFR, MA, ECSA, and carbon dioxide emissions from the cathode exhaust, but these parameters were found to exhibit minimal dependence on crack density (**Figure 3**). The trends of slight increase in ohmic resistance (**Figure 3a**), rapid decrease in

ECSA up to 500 cycles followed by a slower decrease with additional cycles (**Figure 3c**), and rapid increase in amount of carbon lost (**Figure 3d**) are in agreement with previous reports of carbon corrosion effects on CLs.[7] However, cracks were found to have a strong effect on the increase in O_2 transport resistance caused by carbon corrosion, as shown in **Figure 4**. While O_2 transport resistances of the baseline and 2 µm/6 µm CLs were similar at BOT, both the pressure-dependent (slope) and -independent O_2 transport (y-intercept) resistances were drastically lower for the 2 µm/6 µm electrode compared with the baseline electrode at EOT. These results suggest that cracks promote O_2 transport in degraded CLs that have been rendered O_2 transport limited by carbon corrosion and collapse of the native pore structure. Although the authors do not present direct evidence, liquid water transport may also be promoted by the presence of cracks, as suggested by previous works.[48,49]

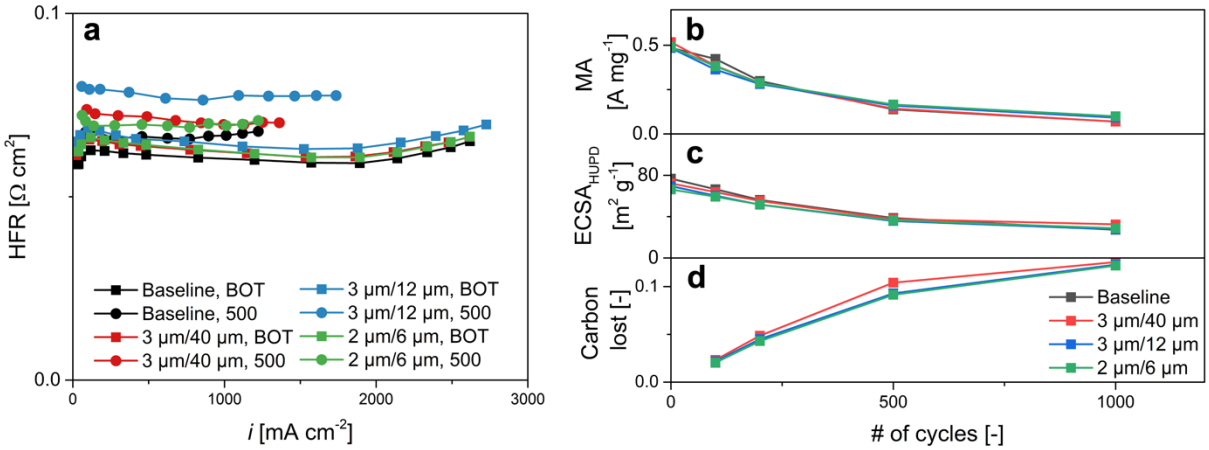

Figure 3. Diagnostics and analysis of MEA and CL properties during carbon corrosion AST. (a) HFR, (b) MA, (c) ECSA, and (d) fraction of carbon lost based on CO_2 emission analysis of the CLs.

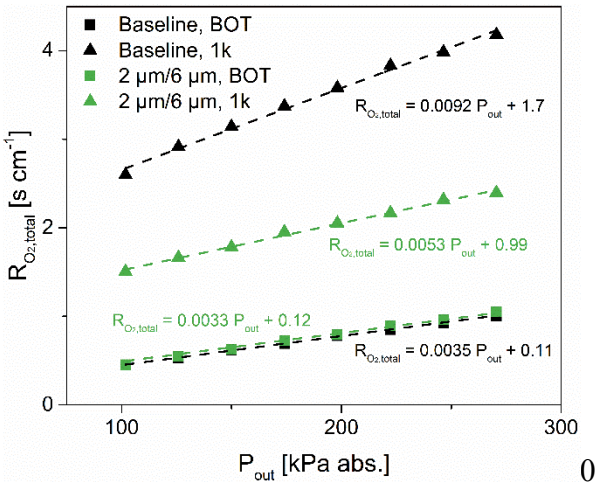

Figure 4. Comparison of oxygen transport resistance measured via limiting current method, for the 2 µm/6 µm and the baseline catalyst layers, at BOT and EOT.

Morphology of catalyst layer with cracks post-carbon corrosion

To provide direct evidence of the role of cracks in promoting O_2 transport in degraded CLs, we imaged the morphology of the CL with cracks before and after carbon corrosion via X-ray computed tomography (CT). Comparing the X-ray CT virtual cross-section of the BOT and EOT samples shown in **Figure 5a,b**, we can initially make two observations about the carbon corrosion effect: the CL became significantly thinner and the contrast between the CL and the adjacent membrane and GDL increased after carbon corrosion. Specifically, while only ~12% of the carbon support was lost to corrosion after 1000 cycles (measured via NDIR, **Figure 3d**), the CL thinned by ~70%, meaning that the decrease in thickness was predominantly driven by deformation and collapse of CL pores. Additionally, the increased contrast suggests that the density of Pt nanoparticles within the voxels that correspond to the CL increased after carbon corrosion. Both of these observations suggest that the AST cycles caused collapse of the native pore structure of the CL, which is consistent with observations made in a previous work.[7] A decrease in CL pore size causes severe limitation in oxygen transport due to reduced Knudsen diffusivity,[50] in agreement with the increase in the pressure-independent O_2 transport resistance presented in **Figure 4**.

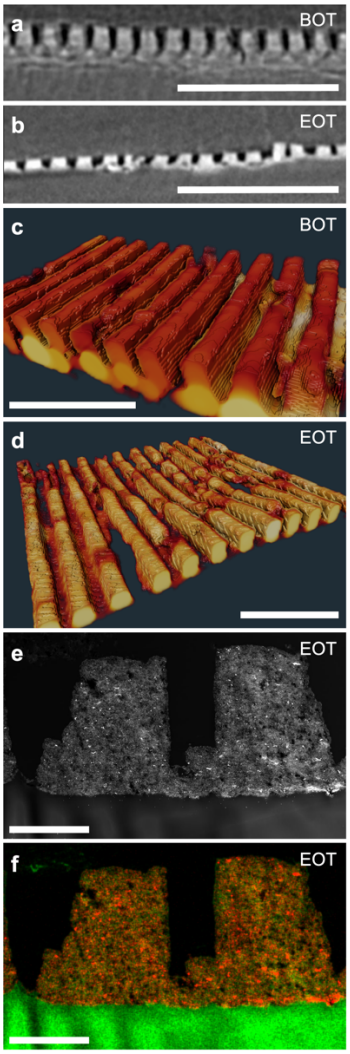

Figure 5. (a-d) Micro CT results of the 3 µm/12 µm electrode at BOT (a,c) and EOT (b,d). The scale bars are 50 µm. (e-f) HAADF-STEM (e) and EDS (f) maps of the 3 µm/12 µm electrode at EOT. Red and green are showing Pt and F, respectively. The scale bars are 5 µm.

Both the micro-CT cross sections and the full 3D reconstructions show that the overall crack morphology remained relatively unaffected by carbon corrosion (apart from crack depth, which scaled with the thinning of the CL thickness) (**Figure 5c,d**). Specifically, the top width of the cracks remained relatively unchanged (2.8 µm to 3.0 µm), while the CL thickness reduced significantly, regardless of the presence of cracks (13.2 µm to 4.2 µm for CL regions without cracks and 5.8 µm to 1.9 µm for CL regions with cracks). The HAADF-STEM images and EDS maps also reveal a relatively uniform spatial distribution of Pt and F without noticeable inhomogeneity in the amount of carbon corrosion (**Figure 5e,f**). Considering that the amount of carbon loss was independent of the crack density (**Figure 3d**), it can be concluded that cracks do not necessarily have a negative impact on carbon support durability. This observation is at odds with a previous report of accelerated crack propagation during potential cycling under H_2/air conditions,[51] suggesting that the specific conditions during carbon corrosion, including

presence or absence of water generation from O_2 reduction, as well as the crack dimensions and morphology (which were kept near-constant in our experiment), may control local carbon corrosion rates. We also did not observe any crack development in the baseline CL, as shown in **Figure S1**, which can be attributed to the relatively crack-free morphology of the catalyst layer at BOT.

We consistently observed that CL cracks were maintained after the carbon corrosion AST, suggesting that they can play a critical role in promoting O_2 diffusion to reaction sites when the CL structure collapses and becomes O_2-transport limited. In a regular baseline CL, net O_2 transport occurs exclusively in the through-plane direction (direction of the CL thickness), whereas in a CL with cracks, net O_2 transport can also occur in the in-plane direction, with O_2 moving laterally from the cracks to access catalytic sites in the adjoining catalyst. This alternative diffusion path can significantly reduce the effective O_2 diffusion length, consequently reducing the oxygen transport resistance (as demonstrated by limiting current measurements in **Figure 4**).

In addition to the positive effect of cracks on PEMFC performance after carbon corrosion, we also observed negligible effects of cracks on catalyst durability, measured via catalyst AST (**Figure S4**). Therefore, our results indicate that cracks have either a positive or neutral effect on CL durability. Previous works have discussed the potential negative impact of CL cracks on membrane durability,[52] and thus for a comprehensive understanding of the effects of CL cracks on MEA durability, future work on mechanical and chemical membrane ASTs is needed, which can be performed using the crack control platform presented in this work.

Conclusions

We systematically investigated the effects of engineered cracks on the carbon corrosion and catalyst durability of PEMFCs. Specifically, we fabricated patterned silicon templates via photolithography and deep-reactive ion etching and used these templates to prepare cathode CLs with precisely-controlled crack density. We observed that the BOT performance was unaffected by the crack density, but the performance was significantly affected when the CL was subjected to carbon corrosion. After 1000 cycles of a carbon corrosion AST, we observed up to 87% higher current density at 0.7 V for the CL with cracks relative to the baseline. Oxygen transport resistance measured via a limiting current technique showed that both the pressure-dependent and -independent resistances were significantly lower for the EOT CL with cracks compared to the EOT baseline. Further investigation via X-ray CT and HAADF-STEM/EDS

showed that the carbon-corroded CLs were severely compacted, causing collapse of the native pore structure and obstructing oxygen transport. In these compacted CLs, the open void space provided by CL cracks facilitates through-plane oxygen transport, resulting in shorter effective oxygen transport distances to the reaction sites. We also demonstrated that cracks have negligible effect on the catalyst durability, evidenced by unaffected polarization curves after catalyst AST. The results of our study provide new insights on how CL cracks affect the performance and durability of PEMFCs.

Acknowledgements

This work was supported by the Hydrogen and Fuel Cell Technologies Office, Office of Energy Efficiency and Renewable Energy, US Department of Energy through the Million Mile Fuel Cell Truck (M2FCT) consortium, technology managers G. Kleen and D. Papageorgopoulos. Financial support for this work from the Laboratory Directed Research and Development program at Los Alamos National Laboratory is gratefully acknowledged (Projects 2020200DR and 20210915PRD2). This work was performed, in part, at the Center for Integrated Nanotechnologies, an Office of Science User Facility operated for the U.S. Department of Energy Office of Science by Los Alamos National Laboratory (Contract 89233218CNA000001) and Sandia National Laboratories (Contract DE-NA-0003525). ChungHyuk Lee acknowledges support from the Natural Sciences and Engineering Research Council of Canada. The Talos F200X S/TEM was provided by U.S.DOE, Office of Nuclear Energy, Fuel Cycle R&D Program, and the Nuclear Science User Facilities.

References

1. K. Jiao et al., *Nature*, **595**, 361–369 (2021).
2. D. A. Cullen et al., *Nat Energy*, **6**, 462–474 (2021).
3. Y.-T. Pan et al., *Chem Catalysis*, **2**, 3559–3572 (2022).
4. L. Cheng et al., *Adv Energy Mater*, **10**, 2000623 (2020).
5. K. Khedekar et al., *Adv Energy Mater*, **11**, 2101794 (2021).
6. H. Yu et al., *Microscopy and Microanalysis*, **28**, 2614–2617 (2022).
7. P. Saha et al., *J Mater Chem A Mater*, **10**, 12551–12562 (2022).
8. L. Hu, B. K. Hong, J.-G. Oh, and S. Litster, *ACS Appl Energy Mater*, **4**, 119–127 (2021).
9. C. Lee et al., *ACS Appl Mater Interfaces*, **14**, 35555–35568 (2022).
10. P. Goyal, A. Kusoglu, and A. Z. Weber, *ACS Energy Lett*, **8**, 1551–1566 (2023).
11. H. Eskandari, V. Ozhukil Kollath, and K. Karan, *The Journal of Physical Chemistry C*, **126**, 17862–17874 (2022).
12. T. Agarwal et al., *J Power Sources*, **554**, 232320 (2023).
13. Y. Chen et al., *J Power Sources*, **520**, 230674 (2022).
14. Y. Chen et al., *J Power Sources*, **520**, 230673 (2022).
15. H. Liu et al., *J Electrochem Soc*, **164**, F704 (2017).
16. M. Balakrishnan et al., *ACS Appl Mater Interfaces*, **13**, 2414–2427 (2021).
17. S. Komini Babu et al., *J Electrochem Soc*, **168**, 024501 (2021).

18. N. Ramaswamy et al., *J Electrochem Soc*, **168**, 124512 (2021).
19. R. L. Borup et al., *Curr Opin Electrochem*, **21**, 192–200 (2020).
20. S. Uemura et al., *J Electrochem Soc*, **166**, F89 (2019).
21. N. Kumano et al., *J Power Sources*, **419**, 219–228 (2019).
22. S. Kundu, M. W. Fowler, L. C. Simon, and S. Grot, *J Power Sources*, **157**, 650–656 (2006).
23. R. T. White et al., *J Electrochem Soc*, **166**, F914 (2019).
24. R. T. White et al., *Sci Rep*, **9**, 1–12 (2019).
25. Q. Guo and Z. Qi, *J Power Sources*, **160**, 1269–1274 (2006).
26. Y. Li et al., *Int J Hydrogen Energy*, **45**, 23519–23525 (2020).
27. Y. Singh, F. P. Orfino, M. Dutta, and E. Kjeang, *J Electrochem Soc*, **164**, F1331 (2017).
28. J. Zhao, S. Shahgaldi, X. Li, and Z. S. Liu, *J Electrochem Soc*, **165**, F3337 (2018).
29. F. E. Hizir, S. O. Ural, E. C. Kumbur, and M. M. Mench, *J Power Sources*, **195**, 3463–3471 (2010).
30. Y. Chang et al., *Energy Convers Manag*, **189**, 24–32 (2019).
31. Y. Singh et al., *Int J Hydrogen Energy*, **44**, 12057–12072 (2019).
32. S. Du et al., *J Electrochem Soc*, **168**, 114506 (2021).
33. D. Ramani et al., *J Power Sources*, **512**, 230446 (2021).
34. D. Ramani et al., *J Power Sources*, **512**, 230431 (2021).
35. D. Ramani, Y. Singh, F. P. Orfino, M. Dutta, and E. Kjeang, *J Electrochem Soc*, **165**, F3200–F3208 (2018).
36. T. G. Tranter, M. Tam, and J. T. Gostick, *Electroanalysis*, **31**, 619–623 (2019).
37. C. Y. Ahn et al., *Sci Rep*, **8**, 1–9 (2018).
38. C. Baez-Cotto et al., in *Electrochemical Society Meeting Abstracts 240*,, p. 1091, The Electrochemical Society, Inc. (2021).
39. C. Lee et al., *Nat Energy*, 1–10 (2023).
40. R. WS, *http://imagej. nih. gov/ij/* (2011).
41. D. R. Baker, D. A. Caulk, K. C. Neyerlin, and M. W. Murphy, *J Electrochem Soc*, **156**, B991 (2009).
42. J. Zhang, L. Paine, A. Nayar, and R. Makharia, *Patent* (2011).
43. USDRIVE, *Fuel Cell Technical Team Roadmap*, (2017).
44. N. Hasegawa, A. Kamiya, T. Matsunaga, N. Kitano, and M. Harada, *Colloids Surf A Physicochem Eng Asp*, **628**, 127153 (2021) https://www.sciencedirect.com/science/article/pii/S0927775721010220.
45. Q. Meyer et al., *Electrochim Acta*, **242**, 125–136 (2017) https://www.sciencedirect.com/science/article/pii/S0013468617310009.
46. S. M. Kim et al., *Sci Rep*, **6**, 26503 (2016).
47. J. Lee, J. Hinebaugh, and A. Bazylak, *J Power Sources*, **227**, 123–130 (2013).
48. Y.-H. Huang, Y.-H. Hsu, and Y.-T. Pan, *ACS Appl Energy Mater*, **5**, 2890–2897 (2022).
49. C.-Y. Ahn et al., *Sci Rep*, **8**, 1257 (2018).
50. W. He, W. Lv, and J. Dickerson, *Gas transport in solid oxide fuel cells*, Springer, (2014).
51. R. T. White et al., *J Power Sources*, **350**, 94–102 (2017).
52. Y. Singh et al., *J Power Sources*, **412**, 224–237 (2019).

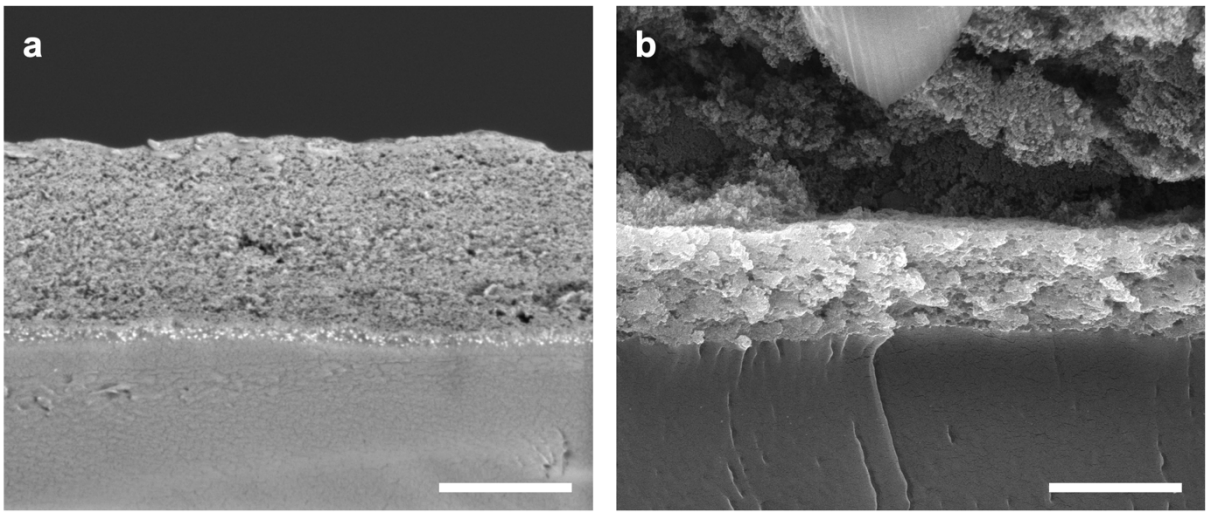

Figure S1. Cross-sectional scanning electron microscopy images of the baseline catalyst layer (free of engineered cracks) at BOT (a) and EOT (b). The scale bars are 5 μm.

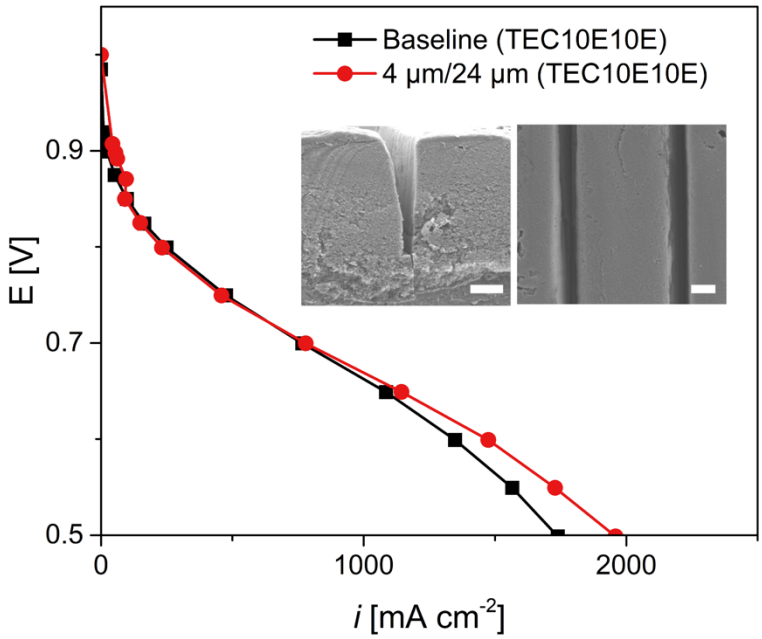

Figure S2. Polarization curves of baseline and 4 µm/24 µm CLs, made with 10 wt.% Pt on high surface area carbon (TEC10E10E, Tanaka Precious Metals), and a cathode loading of 0.10 mg Pt cm^{-2}. The thickness of the CL was ~28 µm. The inset images show (left) cross-section and (right) top view SEM images of a 4 µm/24 µm CL. The scale bars are 5 µm.

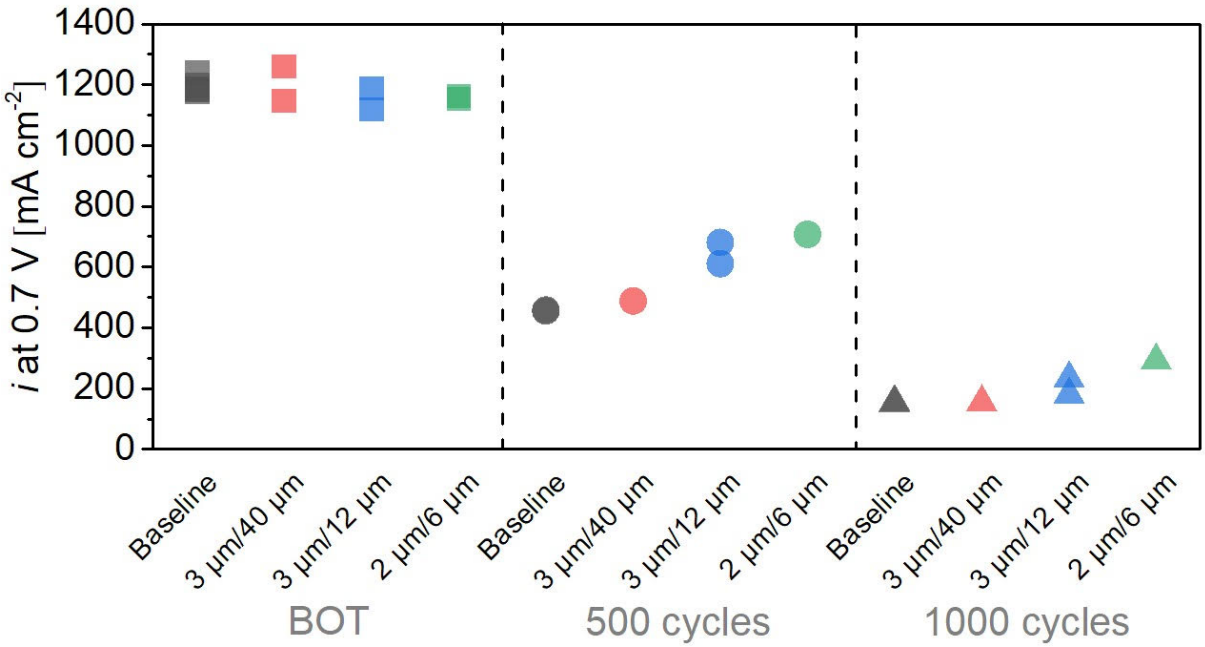

Figure S3. All repeated current density values at 0.7V.

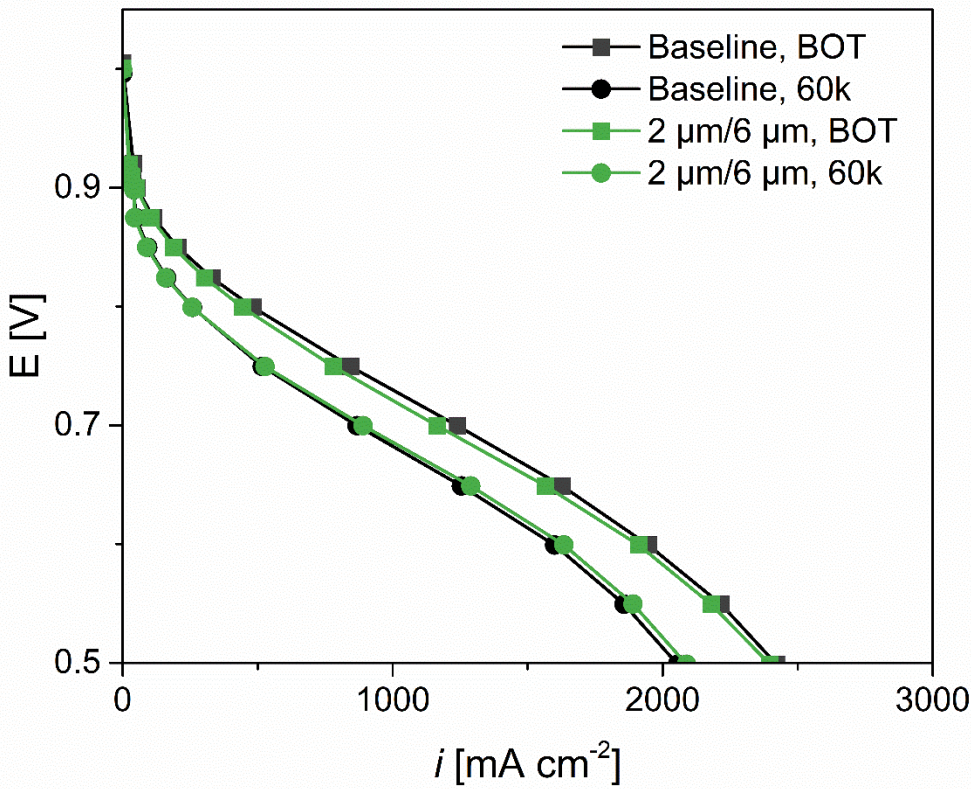

Figure S3. Polarization curves of CLs with and without cracks before and after catalyst AST, under H_2/Air, 1000/3000 sccm, 100% RH, 150 kPa_{abs}, and 80°C.